Journal of Catalysis 438 (2024) 115697

Contents lists available at ScienceDirect

Journal of Catalysis

journal homepage: www.elsevier.com/locate/jcat

Research article

Correlating atomic-scale structural and compositional details of Ca-doped $LaCoO_3$ perovskite nanoparticles with activity and stability towards the oxygen evolution reaction

Fan Bai [a], Jonas Schulwitz [b], Tatiana Priamushko [c], Ulrich Hagemann [d], Aleksander Kostka [e], Markus Heidelmann [d], Serhiy Cherevko [c], Martin Muhler [b], Tong Li [a,*]

[a] Faculty of Mechanical Engineering, Atomic-scale Characterisation, Ruhr-Universität Bochum, Universitätsstraße 150, 44801 Bochum, Germany
[b] Faculty of Chemistry and Biochemistry, Laboratory of Industrial Chemistry, Ruhr-Universität Bochum, Universitätsstraße 150, 44801 Bochum, Germany
[c] Helmholtz-Institute Erlangen-Nürnberg for Renewable Energy (IEK-11), Forschungszentrum Jülich GmbH, Cauerstrasse 1, 91058 Erlangen, Germany
[d] Interdisciplinary Center for Analytics On the Nanoscale (ICAN) and Center for Nanointegration Duisburg-Essen (CENIDE), University of Duisburg-Essen, Carl-Benz-Straße 199, 47057 Duisburg, Germany
[e] Zentrum Für Grenzflächendominierte Höchstleistungswerkstoffe (ZGH), Ruhr-Universität Bochum, Universitätsstraße 150, 44801 Bochum, Germany

ARTICLE INFO

Keywords:
Water electrolysis
Oxygen evolution reaction
Perovskite electrocatalyst
Ca-doped $LaCoO_3$
Atom probe tomography

ABSTRACT

Developing efficient oxygen evolution reaction (OER) electrocatalysts requires a thorough understanding of structure–activity-stability relationships, ideally at the atomic scale. Herein, we employed atom probe tomography and transmission electron microscopy to reveal compositional and structural changes on $LaCoO_3$ and Ca-doped $LaCoO_3$ surfaces during OER. We reveal that the topmost surfaces of pristine perovskite are terminated by the A-site element (La). After OER, amorphous $La(OH)_3$ is formed on the surfaces of $LaCoO_3$, which leads to significant activity deterioration. For Ca-doped $LaCoO_3$, enhanced intercalation and penetration of hydroxide ions, along with the appearance of $Co^{3+/4+}$ redox couple, are observed, contributing to its enhanced OER activity and stability. Our study demonstrates how atomic-scale compositional and structural details of electrocatalyst surfaces deepen our understanding of their activity and stability.

1. Introduction

Water electrolysis is a key technology in the production of hydrogen [1–4]. However, achieving the desired water electrolysis efficiency presents an ongoing challenge, mainly due to limitations in electrocatalyst performance at the anode, where the oxygen evolution reaction (OER) occurs [5]. Perovskite oxides (ABO_3), which incorporate rare-earth or alkaline-earth cations at A-sites and transition metal cations at B-sites, have emerged as effective OER electrocatalysts due to their low cost, high abundance and promising electrocatalytic properties [6]. The flexibility of tuning physicochemical properties by substituting A or B-sites with elements of varying electronegativity, valence and ionic size has led to the development of highly active perovskite electrocatalysts whose OER activity is comparable to the high-cost benchmarks IrO_2 and RuO_2 [6,7]. For example, $LaCoO_3$ exhibits relatively poor OER activity. Partial substitution of La(III) by e.g., Ca(II) and Sr(II), at the A-sites can increase the concentration of oxygen vacancies and improve the OER activity [8–10]. Although Ca-doped $LaCoO_3$ was reported to maintain high OER activity for extended durations (~50 h) [11], it has not yet been well understood how Ca doping affects the structural stability of $LaCoO_3$ during OER. This poor understanding stems from insufficient information regarding the elemental distribution and compositional changes of La, Ca (at the A-sites), Co (at the B-sites), and oxygen in the surface and near-surface regions of the electrocatalysts during OER. In this context, this study will use $LaCoO_3$ and Ca-doped $LaCoO_3$ nanoparticles as model systems to study how surface changes affect their OER activity and stability.

Essentially, optimizing electrocatalysts requires a thorough understanding of the correlation between surface composition, activity and stability. Oxidation state, structure, composition and elemental distribution in the topmost and near-surface region of electrocatalysts all play a decisive role in both activity and stability. However, it is challenging for most characterization techniques to obtain nanometer (nm) or sub-nm scale compositional and elemental details of nanoparticles, in

* Corresponding author.
E-mail address: tong.li@rub.de (T. Li).

https://doi.org/10.1016/j.jcat.2024.115697
Received 1 March 2024; Received in revised form 30 July 2024; Accepted 6 August 2024
Available online 9 August 2024

particular for perovskites, since they often contain multiple substitute elements at the A- or B-sites with low concentrations. Furthermore, the electrocatalyst surfaces undergo drastic and dynamic structural and compositional changes during OER, which alter the activity and stability accordingly. For example, Ba and Sr at the A-sites of $Ba_{0.5}Sr_{0.5}Co_{0.8}Fe_{0.2}O_{3-\delta}$ (BSCF) [12] dissolve during OER, resulting in surface amorphization and formation of active (oxy)hydroxide on the surface. High resolution transmission electron microscopy (HRTEM) [13] and scanning TEM/energy-dispersive X-ray spectroscopy (STEM/EDS) [14] have provided seminal insights into the surface amorphization and compositional changes of perovskites after OER. However, EDS signals originating from the thin surface or near-surface regions of nanometer-sized perovskite nanoparticles suffer from low counts. Furthermore, these surface region signals can overlap with those from the inner regions of nanoparticles, since they are obtained from two-dimensional (2D) images. As a result, the insufficient information regarding elemental distribution and composition in surface and near-surface regions of perovskites hinders a thorough evaluation of the contribution that individual atoms in this extended zone make to the interplay between catalytic activity and stability.

Atom probe tomography (APT) can provide 3D distribution maps of individual atoms and compositional changes in nanoparticles both before and after electrocatalytic reactions with sub-nm spatial resolution [15], as evidenced by our recent work on oxyhydroxide and spinel oxide nanoparticles [16–19]. In this study, we employ a multimodal approach that combines APT with X-ray photoemission spectroscopy (XPS) and HRTEM to characterize sub-nm scale compositional and structural evolution of the topmost surface and near-surface regions of $LaCoO_3$ and Ca-doped $LaCoO_3$ before and after cyclic voltammetry (CV) measurements under OER conditions. The aim of this study is to elucidate the effects of Ca on the structural and compositional changes of $LaCoO_3$ towards OER, thereby clarifying why Ca promotes the stability of $LaCoO_3$. We reveal hydroxide ions (OH^-) were present across Ca-doped $LaCoO_3$ nanoparticles. Dynamic penetration of hydroxide ions coupled with reversible $Co^{3+/4+}$ redox couple is thought to promote both activity and stability of Ca-doped $LaCoO_3$ towards OER.

2. Experimental section

2.1. Synthesis

All chemical reagents used in this work were purchased from Sigma-Aldrich. The ultrapure water purified with the Milli-Q purification system was used to prepare all solutions except special notes. $LaCoO_3$ and Ca-doped $LaCoO_3$ were synthesized using the hydrothermal method. La $(NO_3)_3{\cdot}6H_2O$ (0.151 g, 0.121 g, 0.091 g, 0.060 g), $Ca(NO_3)_3{\cdot}4H_2O$ (0, 0.016 g, 0.033 g, 0.049 g), $Co(NO_3)_3{\cdot}4H_2O$ (0.102 g) and L-ascorbic acid (0.3 g) were dissolved in 18 ml H_2O with magnetically stirring for 30 min to obtain the precursor solution. The solution pH value was adjusted to 8.9 with $NH_3{\cdot}H_2O$. After stirring for 30 min, the solution was transferred to a 25 mL Teflon-lined autoclave and heated at 180 °C for 10 h. The precipitates were washed with pure water and ethanol for five times, and dried at 60 °C for 12 h. The obtained products were further calcined at 600 °C for 2 h in a muffle furnace to form the perovskite phases.

2.2. Electrochemical measurement

All the electrochemical tests were carried out in a standard three electrodes cell with O_2-saturated 1.0 M KOH (pH=14) at a rotation speed of 1600 rpm using a potentiostat (Bio-Logic SP-300). The KOH electrolyte was purified with chelating ion exchange resin (Chelex 100, Bio-Rad) before use to remove metal impurities[20]. A Pt wire was used as a counter electrode, and a Hg/HgO electrode was the reference electrode. The working electrode was prepared as follows: 4 mg electrocatalyst powder was dispersed in the mixture of 705 μL ultrapure water, 250 μL isopropanol and 45 μL Nafion, and sonicated for 30 min. Before electrochemical measurements, a bare glassy carbon electrode (GCE) with a diameter of 5.0 mm was cleaned with alumina slurry and rinsed ultrasonically with ethanol and water for 20 s, successively. 10 μL dispersion was subsequently dropped on the GCE and dried at room temperature, obtaining a catalyst loading of 0.204 mg cm^{-2}.

CV measurements were performed between 0 and 0.73 V (vs. Hg/HgO) with a scan rate of 100 mV/s for 1000 cycles in 1.0 M KOH. The samples for XPS, TEM and APT measurements were prepared using the same electrochemical setup in 1.0 M KOD in D_2O. Linear sweep voltammetry (LSV) was conducted between 0 and 0.86 V (vs. Hg/HgO) with a scan rate of 10 mV/s. Electrochemical impedance spectroscopy (EIS) was performed under OER conditions by applying a sine wave signal with a 10 mV amplitude in the frequency range from 100 kHz to 0.1 Hz after equilibrating 5 s at 0.73 V (vs. Hg/HgO). The uncompensated series resistance (R_s) of the electrode setup is ~ 6 O from Nyquist plots shown in Fig. S1. An ohmic drop (iR_s) correction (95 %) was applied to compensate for the decrease in the actual electrode potential when compared to the nominal potential due to current flux in the highly resistive system [21]. All electrochemical tests were repeated three times. The measured potentials were calculated to the potential vs reversible hydrogen potential according to the equation:

$$E_{RHE} = E_{Hg/HgO} + 0.118 + 0.059 \times pH$$

Oxygen intercalation process and diffusion coefficients (D_O) were investigated in an Ar-saturated 6 M KOH electrolyte at room temperature according to the previous work [10,13]. CV measurements were carried out at various scan rates from 2 mV s^{-1} to 100 mV s^{-1}. Chronoamperometry (CA) was performed by applying a potential 50 mV more anodic of the $E_{1/2}$ (defined as the potential halfway between the peak currents for oxygen insertion and extraction). The electrochemical capacitance was measured by CV between 0.974 V − 1.074 V (vs. RHE) at various scan rates of 25 mV s^{-1}, 50 mV s^{-1}, 75 mV s^{-1}, 100 mV s^{-1} and 125 mV s^{-1}.

2.3. Characterization

X-ray diffraction (XRD) patterns were recorded using a Bruker Discover D8 with a θ- θ geometry and a Lynxeye-1D detector and Cu Kα radiation (λ = 0.15406 nm, 40 kV, 40 mA) in a 2θ range from 10 to 80° with a step size of 0.07° and a time per step of 1.5 s. XPS was tested on a Versa Probe II (Ulvac-Phi) using a monochromatic Al X-ray source (1486.6 eV) operating at 15 kV and 13.2 W. After the electrochemical cycling, the samples were washed with ultrapure water immediately to remove the residual electrolyte and stored in the glove box. The prepared samples were quickly transferred to the XPS instrument to avoid oxidation from air. TEM and HRTEM images were taken in an aberration-corrected JEOL JEM-2200FS operating at 200 kV. TEM/EDS was performed in STEM mode of an aberration-corrected JEOL JEM-ARM200F NEOARM equipped with two 100 mm^2-sized EDS detectors. The Brunauer-Emitter-Teller (BET) specific surface areas were obtained by N_2 physisorption measurements using a BEL-mini apparatus at 77 K.

To prepare the APT specimens, the nanoparticles were embedded in the Cu matrix on a Cu plate using an electrodeposition process at a voltage of −0.50 V (vs Ag/AgCl) for 8 min in 0.25 M $CuSO_4$ electrolyte. This electrodeposited Cu plate was subsequently used to prepare needle-shaped APT specimens by a lift-out procedure using a focus ion beam/scanning electron microscope (FEI Helios G4 CX). The APT experiments were conducted in CAMECA LEAP 5000XR instrument in laser pulsing mode with a specimen temperature of 57 K, laser energy of 30 pJ, pulse frequency of 125 kHz, and detection rate of 0.5. The APT data was reconstructed and analyzed using the commercial AP Suite 6.3 software.

The La, Co, and Ca amounts in the electrolytes were analyzed by inductively coupled plasma mass spectrometry (ICP-MS, PerkinElmer NexION 350 ×). ICP-MS was calibrated before the measurements by a

four-point calibration slope prepared from standard solutions that contained ^{40}Ca, ^{59}Co and ^{139}La. ^{74}Ge and ^{140}Ce standards were used as internal standards. The internal standard solution was prepared in pure 2 % HNO_3 electrolyte and introduced to the nebulizer of the ICP-MS via a Y-connector. Because of the presence of ^{40}Ca, the ICP-MS was operated in a dynamic reaction cell mode using CH_4 (4.5, Air Liquide) to minimize the impact of the interference with ^{40}Ar. The details for the gas flow and RPq parameters obtained during the optimization and used for all the measurements are listed in Table S1. Moreover, to avoid Ca contamination from the laboratory environment, all the centrifuge tubes used for the sample preparation and measurements were pre-cleaned several times with pure 2 % HNO_3 and water before the measurements. For the elemental analysis, 1 mg of each sample was dissolved in 2 ml of concentrated HNO_3 (65 %, Sigma-Aldrich), which was diluted 10,000 times to be analyzed with ICP-MS. To analyze the amounts of the dissolved elements, 1 M KOH electrolyte was diluted 100 times to be analyzed with ICP-MS. To ensure reproducibility, two samples were prepared for each material, and each sample was measured twice. The dilution factors, as well as the original volumes of the provided analytes, were considered during the evaluation of the results.

The H_2 temperature-programmed reduction (H_2 TPR) measurement were conducted in a flow set-up consisting of a gas supply, a stainless-steel U-tube reactor heated in a ceramic tube furnace, and a thermal conductivity detector (TCD, Hydros 100). For the measurement, ~0.1 g

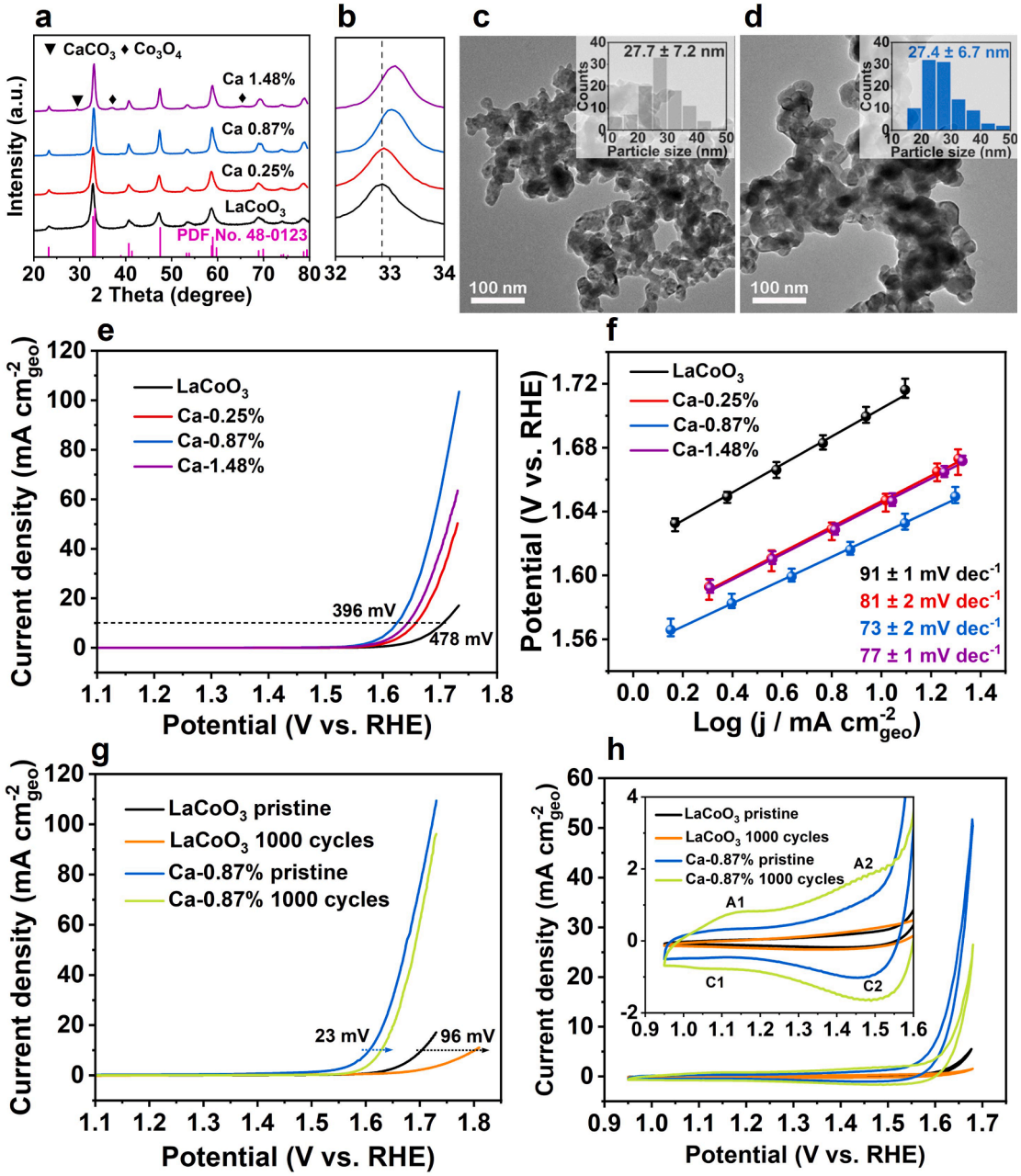

Fig. 1. (a) X-ray diffraction patterns of $LaCoO_3$, Ca-0.25 %, Ca-0.87 % and Ca-1.48 % doped $LaCoO_3$, which can be indexed to a rhombohedral $LaCoO_3$ perovskite structure (PDF card No. 48–0123) with a space group of R-3c(1 6 7). (b) enlarged diffraction peaks between 32–34 degree from (a). TEM images of (c) $LaCoO_3$, (d) Ca-0.87 % doped $LaCoO_3$ and size histograms (insets). (e) LSV and (f) Tafel curves of $LaCoO_3$, Ca-0.25 %, Ca-0.87 % and Ca-1.48 % doped $LaCoO_3$. The error bars were obtained from three measurements for each sample. (g) LSV and (h) CV curves of $LaCoO_3$ and Ca-0.87 % doped $LaCoO_3$ before and after 1000 CV cycles. All electrochemical results were recorded in 1.0 M purified KOH using glassy carbon electrodes deposited with corresponding catalysts at a scan rate of 10 mV/s for LSV and 100 mV/s for CV.

catalyst nanoparticles were pre-treated in 50 Nml min^{-1} He (99.9999 %) at 400 °C for 1 h. After cooling to 60 °C, the set-up was flushed with 50 Nml min^{-1} 4.69 % H_2 (99.9999 %)/Ar (99.9995 %) for 1 h. The furnace was heated to 800 °C with a heating rate of 10 °C min^{-1}. The maximum temperature was kept constant for 1 h. The sample temperature was measured every two seconds by a thermocouple placed inside the reactor. The measured H_2 consumption and temperature were plotted against the measurement time.

3. Results and discussion

Three Ca-doped $LaCoO_3$ with varying Ca doping were prepared. The Ca content is ~ 0.25 at.%, 0.87 at.% and 1.48 at.% measured by TEM/EDS (Table S2 and Fig. S2). For simplicity, we termed the Ca-doped samples Ca-0.25 %, Ca-0.87 % and Ca-1.48 %. The low Ca doping contents can be attributed to the high solubility of Ca(II) in the alkaline solution of the hydrothermal process. In contrast, La(III) and Co(II) are much easier to precipitate due to the lower solubility of $La(OH)_3$ and $Co(OH)_2$ than $Ca(OH)_2$ [22–24]. The La/Co ratio and Ca/La ratio of Ca-0.87 % sample were also measured by ICP-MS, shown in Table S3, which agrees with the EDS results (Table S2). Our X-ray diffraction (XRD) data, in Fig. 1a, shows that $LaCoO_3$ and Ca-doped $LaCoO_3$ samples have a rhombohedral $LaCoO_3$ structure (R-3c) [25]. With increasing Ca concentration, the diffraction peak at ~ 33 degrees shifts to higher values (Fig. 1b). This result suggests that Ca was doped into $LaCoO_3$ by replacing La, albeit low concentrations, since Ca^{2+} has a smaller ionic radius (1.34 Å) compared to La^{3+} (1.36 Å) [26–28]. As the Ca concentration further increases to 1.48 at. %, impurity peaks corresponding to $CaCO_3$ and Co_3O_4 start to appear; the impurity peaks become more pronounced when more than 1.48 at.% Ca was doped (results not shown). The average sizes of $LaCoO_3$ and Ca-doped $LaCoO_3$ (Ca-0.87 %) nanoparticles are similar, ~27 nm, as revealed by the TEM images in Fig. 1c-d. Note that particular effort was required to synthesize relatively small nanoparticles for APT measurements by adding ascorbic acid during the hydrothermal process [29] due to the limited field-of-view of APT (~30–100 nm) [30].

Next, we assessed the effect of Ca doping concentration on OER activity by LSV with pristine $LaCoO_3$, Ca-0.25 %, Ca-0.87 % and Ca-1.48 % doped $LaCoO_3$ using a scan rate of 10 mV/s on a rotating disk electrode (RDE) in 1.0 M KOH under OER conditions. Before electrochemical measurements, KOH was purified to remove the Fe(III) impurities, as even 0.1 ppm Fe in electrolyte could enhance the OER activity of $LaCoO_3$ and $LaNiO_3$ perovskites [31,32]. The current density was normalized to the geometric surface area of the glassy carbon electrodes. The electrochemical active surface areas (ECSA) were not used to estimate the surface areas since the double-layer capacitance of $LaCoO_3$ and Ca-doped $LaCoO_3$ could be overestimated due to their pseudocapacitor characteristics [33]. The LSV plots shown in Fig. 1e reveal that Ca-0.87 % doped $LaCoO_3$ has the highest OER activity, with the lowest overpotential of 396 mV at a current density of 10 mA cm^{-2}, which is lower than that of $LaCoO_3$ (478 mV), Ca-0.25 % (428 mV) and Ca-1.48 % (414 mV) doped $LaCoO_3$. These results indicate that the OER activity of Ca-doped $LaCoO_3$ increases with Ca doping concentration when Ca $\leq$ 0.87 at.%; beyond this threshold, OER activity decreases. This finding is consistent with previous studies that showed a remarkable improvement in OER activity after doping Ca in $LaCoO_3$ even at low concentrations [6,34]. Moreover, Ca-0.87 % doped $LaCoO_3$ exhibits a lower Tafel slope (73 ± 2 mV dec^{-1}) compared to $LaCoO_3$ (91 ± 1 mV dec^{-1}), Ca-0.25 % (81 ± 2 mV dec^{-1}) and Ca-1.48 % (77 ± 1 mV dec^{-1}) samples, Fig. 1f, indicating that Ca-0.87 % doped $LaCoO_3$ exhibits faster charge transfer kinetics than $LaCoO_3$ and other Ca-doped $LaCoO_3$ nanoparticles [35]. In addition, $LaCoO_3$ and Ca-0.87 % doped $LaCoO_3$ exhibit similar BET areas of 22.1 m^2 g^{-1} and 23.0 m^2 g^{-1}, respectively (Fig. S3a). The LSV curves normalized to the BET further suggest the Ca-0.87 % doped $LaCoO_3$ exhibits higher OER activity than $LaCoO_3$ (Fig. S3b).

In addition to activity in the pristine state, we investigated activity changes by performing LSV on the $LaCoO_3$ and Ca-0.87 % doped $LaCoO_3$ after 1000 CV cycles in the range of 0.944 V − 1.674 V vs. RHE at a scan rate of 100 mV/s. The LSV data presented in Fig. 1g shows that the overpotential of Ca-0.87 % doped $LaCoO_3$ measured at 10 mA cm^{-2} increased only by 23 mV after 1000 cycles, which is in stark contrast to the considerable overpotential increase of 1000-cycle treated $LaCoO_3$ (96 mV) and Ca-0.25 % doped $LaCoO_3$ (53 mV in Fig. S4). These results suggest that an optimal Ca doping slows down the activity deterioration of $LaCoO_3$. Additionally, Ca-0.87 % doped $LaCoO_3$ exhibits relatively pronounced redox couples during the CV measurements compared to $LaCoO_3$ (Fig. 1h). Two pairs of redox waves (A1/C1 and A2/C2) were observed between 1.0–1.2 V and 1.4–1.55 V in the CV curve of Ca-0.87 % doped $LaCoO_3$, which can be assigned to Co(II, III) ↔ Co(III) and Co(III) ↔ Co(III, IV) according to the previous reports [36,37]. Interestingly, such redox couples and the enclosed area of CV curves become more intensified after 1000 cycles (green curve in Fig. 1h). This possibly arises from enhanced incorporation and intercalation of hydroxide ions in the Ca-0.87 % doped $LaCoO_3$ during OER. To further confirm the different degrees of hydroxylation, we performed CV measurements $LaCoO_3$ and Ca-0.87 % doped $LaCoO_3$ at various scan rates (Supplementary Note 1 and Fig. S5). We observed that the redox features are highly dependent on the scan rates (Fig. S5a-c), suggesting these peaks are attributed to not only Co(III)/Co(IV) redox couples but also oxygen intercalation/de-intercalation [10,13]. The redox features of Ca-0.87 % doped $LaCoO_3$ are higher than that of $LaCoO_3$ at each scan rate, which indicates that the more robust oxygen intercalation/de-intercalation behavior of Ca-doped $LaCoO_3$ (Fig. S5d). The oxygen intercalation/de-intercalation process of Ca-doped $LaCoO_3$ most likely occurs via the following reactions (1–2),

$$La_{1-x}Ca_xCo^{II,III}O_{3-\delta} + 2\sigma OH^- \rightleftharpoons La_{1-x}Ca_xCo^{III}O_{3-\delta+\sigma} + \sigma H_2O + 2\sigma e^- \quad (1)$$

$$La_{1-x}Ca_xCo^{III}O_{3-\delta} + 2\sigma OH^- \rightleftharpoons La_{1-x}Ca_xCo^{III,IV}O_{3-\delta+\sigma} + \sigma H_2O + 2\sigma e^- \quad (2)$$

Further, according to the previous work [10,13], we measured the oxygen diffusion coefficient from our chronoamperometry data (see Fig. S5e and Supplementary Note 1). The oxygen ion diffusion in Ca-0.87 % doped $LaCoO_3$ is about six times faster than in $LaCoO_3$, most likely leading to the enhanced incorporation and intercalation of hydroxide ions in Ca-doped sample during OER. This also explains the faster charge transfer kinetics of Ca-0.87 % sample, as indicated by the Tafel slopes (Fig. 1f). The enhanced oxygen intercalation/de-intercalation process is also accompanied by an increase in electrochemical capacitance (pseudocapacitance) of Ca-0.87 % doped $LaCoO_3$ after 1000 cycles (Fig. S6). In comparison, the electrochemical capacitance of $LaCoO_3$ decreased by 60 % after 1000 cycles. The increased electrochemical capacitance of Ca-0.87 doped $LaCoO_3$ may also result from surface reconstruction accompanied by A-site metals dissolution [12,38], which is investigated in the following section.

In summary, Ca-0.87 % doped $LaCoO_3$ exhibits better activity and stability towards OER compared to $LaCoO_3$. To determine the origins of the high activity and stability improvement of Ca-0.87 % doped $LaCoO_3$, and the degradation of $LaCoO_3$, we employed XPS, HRTEM and APT to investigate and compare the oxidation state, structure and composition of both perovskites before and after OER. Fig. 2 presents La $3d_{5/2}$ and Co $2p$ spectra of $LaCoO_3$ and Ca-0.87 % doped $LaCoO_3$, both in the pristine state and after 1000 CV cycles under OER conditions (Ca 2p spectra shown in Fig. S7 [39] and surface concentration measured by XPS summarized in Table S4). We can see from Fig. 2a that the La $3d_{5/2}$ spectra of $LaCoO_3$ after 1000 cycles show slight changes compared to its pristine state. In contrast, the La $3d_{5/2}$ spectra of Ca-0.87 % doped $LaCoO_3$ remain similar after 1000 cycles. To distinguish the changes of La oxidation state in $LaCoO_3$ after OER, the La $3d_{5/2}$ spectra were fitted by three components: $c4f^0$ (the final state without charge transfer), $c4f^1$ bonding and $c4f^1$ antibonding (bonding and antibonding component of the final state with charge transfer from O $2p$ state band to empty $4f$ orbital), where c represents the presence of a core hole [40,41]. From the fitting result (Fig. S8 and Table S5), for $LaCoO_3$ after 1000 cycles, both the separation of the $c4f^0$ to $c4f^1$ bonding and $c4f^1$ bonding to $c4f^1$

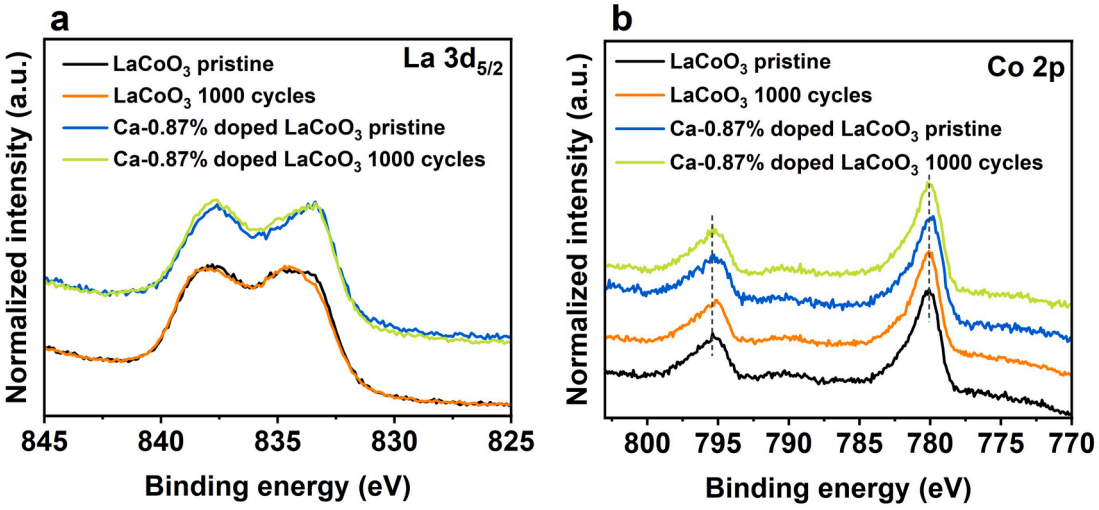

Fig. 2. (a) XPS La $3d_{5/2}$ spectra and (b) Co 2p spectra of $LaCoO_3$ in pristine state and after 1000 CV cycles and Ca-0.87% doped $LaCoO_3$ in pristine state and after 1000 CV cycles. The peak fitting of La $3d_{5/2}$ spectra can be found in Fig. S8.

antibonding decrease compared to the pristine state, indicating the formation of $La(OH)_3$ on the surface of $LaCoO_3$ during OER [41,42]. It is generally accepted that the A-site cation (i.e., La) of perovskite is not active, and, instead, the B-site cation (Co) and its redox couple play decisive roles in the OER activity[43,44]. To interrogate the Co oxidation state, we measured the binding energy of Co $2p_{1/2}$ and Co $2p_{3/2}$, presented in Table S6. Co(II) and Co(III) could be differentiated by the $Co2p_{1/2}$–$2p_{3/2}$ spin–orbit level energy spacing with 16.0 eV for high-spin Co(II) and 15.0 eV for low-spin Co(III) [45,46]. Compared to $LaCoO_3$, the Ca-0.87 % doped $LaCoO_3$ has a higher binding energy difference (~15.5 eV), indicating the existence of more Co(II). A decrease in the Co oxidation state is most likely caused by the creation of oxygen vacancies after Ca doping for maintaining overall charge neutrality. This was confirmed by the fitting results of O 1 *s* spectra (Fig. S9 and Table S7) where an increased O2/O1 ratio of Ca-0.87 % doped sample indicates its higher oxygen vacancy concentration than $LaCoO_3$ [13,35]. Our observation is consistent with the previous work that Ca^{2+} substitution in $LaCoO_3$ can increase Co 3d-O 2p covalency and lower the Fermi level to the Co 3d π*- O 2p π * band, leading to the formation of ligand hole, whereby O_2 could be released from the lattice and form oxygen vacancies [10,34]. After 1000 CV cycles, the decreased binding energy difference (15.2 eV) suggests an increased oxidation state of Co. Additionally, Ca concentration and Ca/La ratio decrease after 1000 cycles (measured from the XPS data and summarized in Table S4), implying Ca dissolution during OER.

To further elucidate the reasons for the activity decrease in $LaCoO_3$ and high stability of Ca-0.87 % doped $LaCoO_3$, other factors, such as structural transformation and compositional changes, were subsequently investigated by HRTEM and APT.Fig. 3 shows the HRTEM images of $LaCoO_3$ and Ca-0.87 % doped $LaCoO_3$ before and after 1000 CV cycles. Both samples in the pristine state exhibit the characteristic lattice fringes of the perovskite rhombohedral structure (R-3c) on the surface and in the bulk of the nanoparticles (Fig. 3a-b). After 1000 CV cycles, the surface 4–5 nm region of $LaCoO_3$ becomes amorphous, as shown from 13 out 16 nanoparticles in Fig. 3c,e and Fig. S10. Surface amorphization is generally attributed to the formation of active oxyhydroxide, along with A-site leaching of perovskites whose O 2p-band is near the Fermi level, such as BSCF, where the lattice oxygen redox mechanism dominates [47]. For instance, Sr-substituted $LaCoO_3$ underwent structural changes and surface amorphization due to Sr leaching during OER [31,42]. To examine if the surface amorphization observed in this study is induced by the cation leaching in $LaCoO_3$, ICP-MS was performed to measure the analyte concentrations after OER. Table S8 shows that negligible amounts of La and Co dissolve in the electrolyte after OER cycling at pH 14. As a result, surface amorphization of $LaCoO_3$ is not induced by La dissolution. In addition, the stability number (S-number), defined by the ratio of the amount of evolved oxygen and the amount of dissolved active atoms, could be a metric to evaluate the activity versus stability, according to the previous report[48]. We measured the S-number (Supplementary Note 4) and found out that Ca-0.87 % doped $LaCoO_3$ has a higher S-number, which further demonstrates its better OER stability than $LaCoO_3$. To investigate the origins of surface amorphization, selected area electron diffraction (SAED) patterns were recorded from hundreds of nanoparticles before and after 1000 CV cycles (Fig. S12a,c). After 1000 cycles, additional reflection spots corresponding to (1 0 0) and (1 0 1) planes of $La(OH)_3$ (JCPDS: 36–1481) were observed (Fig. S12c). This result suggests that the pronounced surface amorphization of $LaCoO_3$ likely arises from the formation of $La(OH)_3$, which is consistent with our XPS data (Fig. 2a). The surface transformation into $La(OH)_3$ decreases the OER activity of $LaCoO_3$ since $La(OH)_3$ is inactive for OER [42]. Note that the pristine $LaCoO_3$ also contains a secondary La_2O_3 phase, as indicated by additional reflection spots in Fig. S12a, while the secondary phase has only a low volume fraction (< ~5%) as it is indiscernible by our XRD data (Fig. 1a).

Compared to $LaCoO_3$, the surface of Ca-0.87 % doped sample remains crystalline after OER, as revealed by 16 out 20 nanoparticles in Fig. 3d,f and Fig. S11. According to XPS (Table S4), Ca dissolution occurs. Also, Ca-doped $LaCoO_3$ possibly contains oxygen vacancies. Both possibly lead to the hypothesis that surfaces of Ca-doped $LaCoO_3$ would be amorphous by forming an active $CoO_x(OH)_y$ layer, as reported in previous studies [31,42]. However, such surface amorphization of Ca-doped $LaCoO_3$ was not observed in our study. To further verify this, we also recorded the SAED of Ca-0.87 % doped $LaCoO_3$ before and after OER (Fig. S12b, d), which show that all diffraction rings after 1000 cycles correspond to $LaCoO_3$ structure (R-3c) (Fig. S12d). Notably, previous operando X-ray-based spectroscopy studies [49,50] reported that the surfaces of Co spinels transformed to a highly reversible X-ray amorphous $CoO_x(OH)_y$ layer that promotes OER activity. Thus, we speculate that surface transformation of the Ca-doped $LaCoO_3$ into $CoO_x(OH)_y$ most likely occurs but reversibly, making capturing this layer by ex-situ TEM challenging after OER cycling. Additionally, we cannot exclude the possibility that the electron beam in TEM induced structural changes in the surface of the Ca-doped sample.

To investigate the elemental redistribution and compositional changes, we employed APT to resolve surface compositions of $LaCoO_3$ and Ca-0.87 % doped $LaCoO_3$ before and after 1000 CV cycles (mass spectra shown in Fig. S13). Electrochemical measurements were conducted using deuterated electrolyte (1 M KOD in D_2O) to investigate the

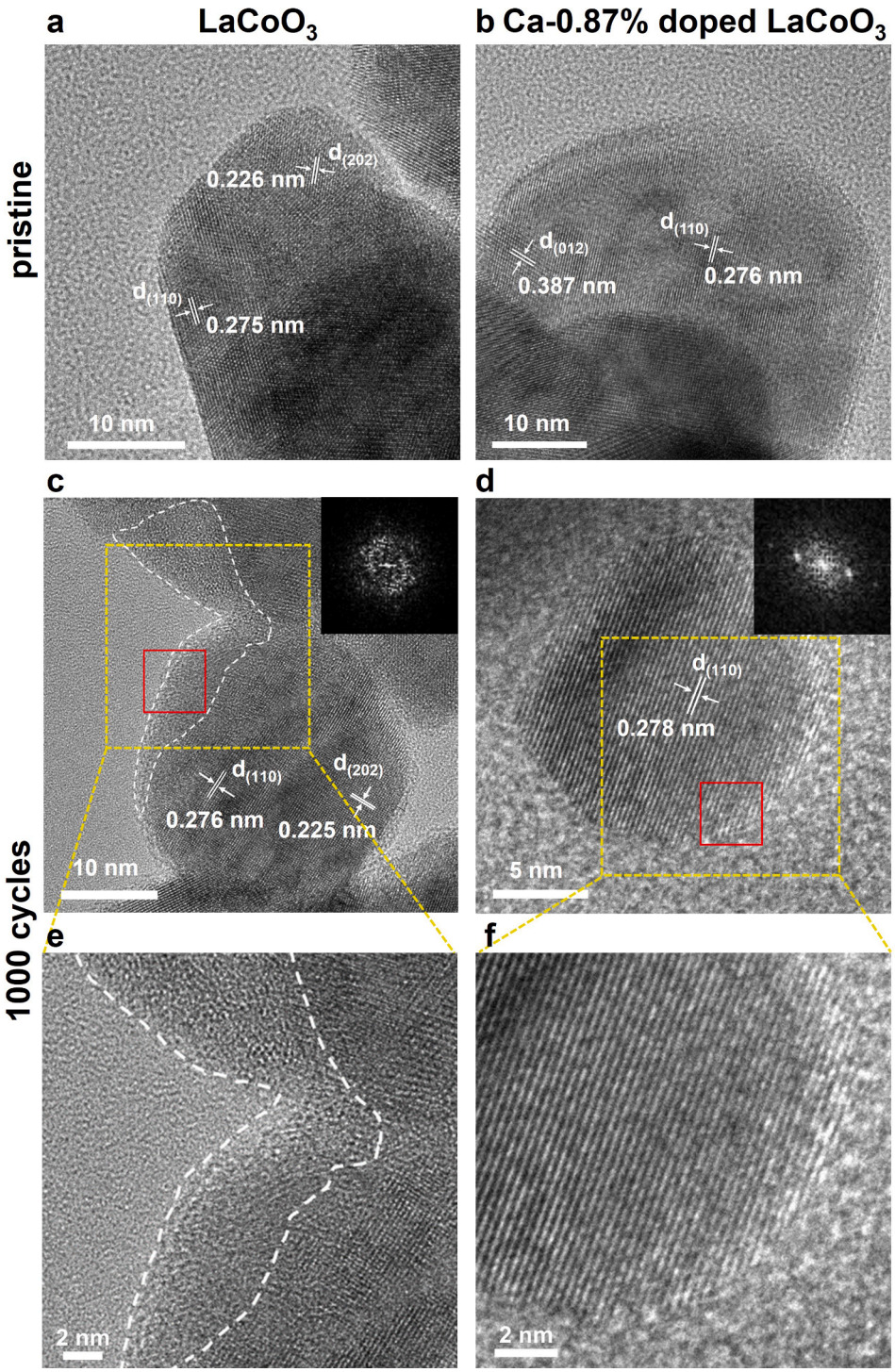

Fig. 3. Surface structural evolution of $LaCoO_3$ and Ca-0.87% doped $LaCoO_3$. High-resolution TEM images of $LaCoO_3$ and Ca-0.87% doped $LaCoO_3$ (a,b) before and (c, d) after 1000 CV cycles. Insets in (c,d) are fast Fourier transforms (FFT) from the responded red areas. (e,f) Magnified TEM image of nanoparticle surfaces in (c,d). Crystalline surfaces are observed for both pristine samples. After 1000 cycles, a thick amorphous area (white line region) is observed at the surface of $LaCoO_3$ nanoparticles, while Ca-0.87% doped $LaCoO_3$ still exhibits a crystalline surface.

distribution of hydroxyl groups after OER [51]. The pristine and post-OER perovskite nanoparticles were embedded in a Cu matrix through electrodeposition to prepare the needle-like APT specimens; the nanoparticles embedded in the Cu matrix and a Ni matrix was compared and discussed in Supplementary Note 2 and Fig. S14). Fig. 4a presents the atom map of a pristine $LaCoO_3$ nanoparticle. $LaCoO_3$ nanoparticles have an overall La/Co ratio of 1.4, summarized in Table 1, which is close to the La/Co ratio of 1.46 obtained from the ICP-MS result (Table S3). Interestingly, the topmost surface (~3 nm region) of the $LaCoO_3$ nanoparticle, shown in Fig. 4a, exhibits a slightly higher La/Co ratio (~1.5) compared to its bulk region (~0.97), as indicated by the 1D concentration profile depicted in Fig. 4b. This suggests that La dominates the topmost surface of $LaCoO_3$ at the A-sites, consistent with previous reports that La is enriched on the surfaces of $LaCoO_3$ perovskite [26,52,53]. After 1000 CV cycles, the overall La/Co ratio of $LaCoO_3$ increases to ~ 1.7 (Fig. 4c-d and Table 1, Fig. S15), possibly due to the

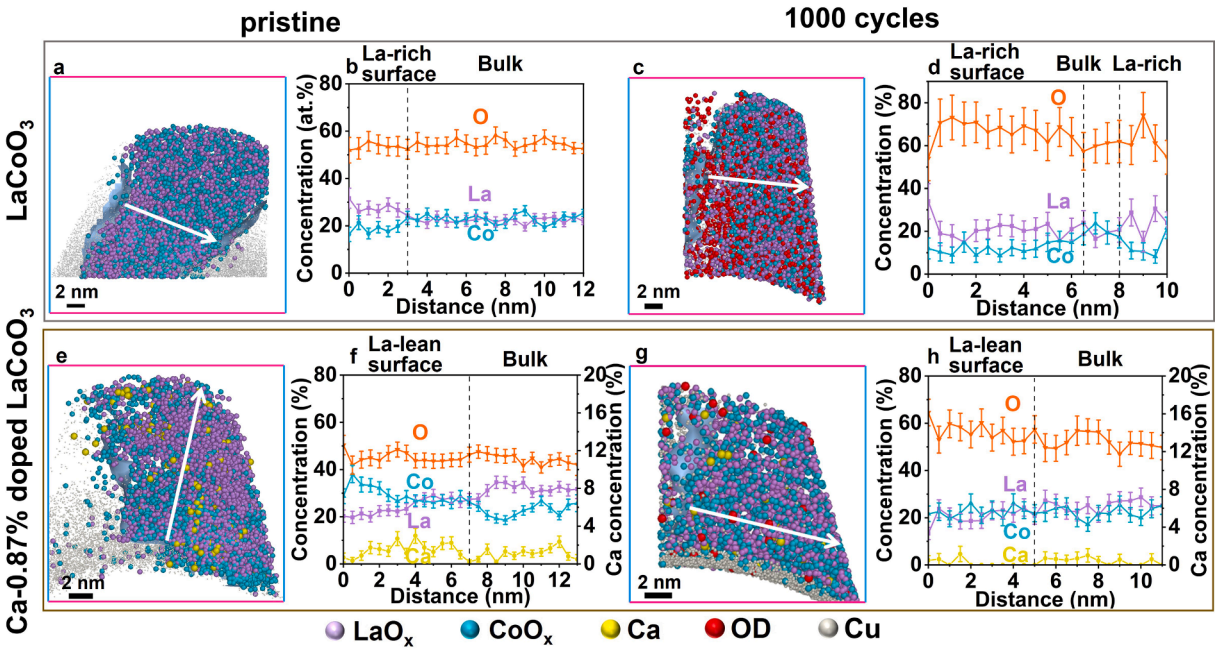

Fig. 4. Cross-sectional atom maps of (a, c) $LaCoO_3$ and (e, g) Ca-0.87% doped $LaCoO_3$ nanoparticles in pristine state and after 1000 CV cycles embedded in the Cu matrix. (b, d, f, h) corresponding 1D concentration profiles plotted along the white arrows. The corresponding La/Co and Ca/La ratio are plotted in Fig. S15.

Table 1
Calculated O concentration, OD concentration and atom ratios from APT results.

Sample and region[a]			La/Co ratio[b]	O concentration (at. %)[c]	Ca/La ratio	OD concentration (at. %)
$LaCoO_3$	Pristine	total	1.4 ± 0.1	53.4 ± 0.1	–	–
		Bulk	0.97 ± 0.1	54.5 ± 0.7	–	–
		La-rich	1.5 ± 0.1	53.8 ± 1.7	–	–
	1000 cycles	total	1.7 ± 0.1	63.9 ± 0.8	–	9.3 ± 0.3
		Bulk	0.98 ± 0.18	59.9 ± 4.4	–	11.6 ± 0.1
		La-rich	1.8 ± 0.2	65.9 ± 2.2	–	9.9 ± 0.1
Ca-0.87 % doped $LaCoO_3$	Pristine	total	0.91 ± 0.01	48.9 ± 0.1	0.054 ± 0.001	–
		La-lean	0.86 ± 0.03	45.1 ± 0.8	0.062 ± 0.006	–
		Bulk	1.4 ± 0.1	44.4 ± 0.8	0.037 ± 0.004	–
	1000 cycles	total	1.0 ± 0.1	54.3 ± 1.1	0.014 ± 0.004	0.22 ± 0.07
		La-lean	0.91 ± 0.06	56.9 ± 1.7	0.010 ± 0.005	0.31 ± 0.13
		Bulk	1.1 ± 0.07	52.0 ± 1.5	0.016 ± 0.005	0.14 ± 0.08

[a] The total regions were the overall APT data of each sample. The bulk and La-rich regions were selected from the corresponding 1D concentration profiles in Fig. 4.

[b] The error bars for the ratio were calculated from $R\sqrt{(\frac{\sigma_i}{c_i})^2+(\frac{\sigma_j}{c_j})^2}$, where R is the ratio of i/j. [c]The concentrations were calculated from $c_i = \frac{n_i}{n}$ and the error bars for the concentrations were calculated from $\sigma_i = \frac{\sqrt{n_i}}{n}$, where n_i is the total number of atoms of element i and n is the total number of all atoms.

Co dissolution (Table S8). Additionally, the surface La-rich regions in $LaCoO_3$ have a higher number of oxygen (~65.9 at.%) and hydroxide ions (~9.3 at.%, see Table 1), further confirming the formation of $La(OH)_3$. By relating the finding of HRTEM and SAED results (Fig. 3a,c), we conclude that the surface amorphization of $LaCoO_3$ likely arises from transformation into $La(OH)_3$, which acts as an inactive passivation film, leading to significant electrocatalyst degradation after prolonged OER cycling [42]. Previous work reported that $LaCoO_3$ exhibits high structural stability [12], where the $LaCoO_3$ surface structure remained crystalline after OER at pH 13. In our study, the surface transformation to $La(OH)_3$ is possibly induced by higher pH (14). Additionally, from a thermodynamic perspective, it should be noted that $La(OH)_3$ is the stable phase of La in alkaline media upon CV cycling in our potential range according to the La Pourbaix diagram [54].

In comparison to $LaCoO_3$, pristine Ca-0.87 % doped $LaCoO_3$ shows a La/Co ratio of ~ 0.91 (Fig. 4e-f) and the Ca/La ratio in Ca-0.87 % doped $LaCoO_3$ is ~ 0.054 (with a Ca concentration of ~ 1.4 at.%, Table 1), which is close to the ICP-MS data (Table S3). Interestingly, the oxygen concentration in pristine Ca-0.87 % sample is ~ 48.9 at.%, lower than that in pristine $LaCoO_3$ (53.4 at.%) (Fig. 4e-f, Table 1). This result infers that Ca(II) substitution of La(III) in $LaCoO_3$ generates oxygen vacancies to maintain the charge neutrality. This is consistent with our XPS data (O 1 s spectra in Fig. S9, Table S7), where an increased O2/O1 ratio is observed for Ca-0.87 % doped $LaCoO_3$ than that in $LaCoO_3$, implying the existence of more oxygen vacancies [13,35]. We are aware that the absolute intensities or ratios of XPS spectra might vary between experiments due to the surface adsorbates or contaminates. Oxygen concentration measured by APT only gives atomic percentages of elements. Thus, we further performed the H_2 TPR measurement (Supplementary Note 3 and Fig. S16) to interrogate the oxygen vacancies. The results in Fig. S16 show that Ca-0.87 % doped $LaCoO_3$ exhibits a lower surface reduction temperature than $LaCoO_3$, suggesting the enhanced oxide reducibility of Ca-0.87 % doped $LaCoO_3$. The lower surface reduction temperature is an indicator of a lower surface oxygen vacancy formation energy [55], which implies that oxygen vacancies are more easily formed in Ca-0.87 % doped $LaCoO_3$ than $LaCoO_3$. This provides an

indirect evidence that more oxygen vacancies are likely present in Ca-0.87 % doped $LaCoO_3$, explaining the low oxygen content revealed by our APT data.

Additionally, the APT data in Fig. 4e-f, reveals that Ca (yellow spheres) is distributed unevenly across the Ca-0.87 % doped $LaCoO_3$ nanoparticles. Ca has a relatively higher concentration in the La-lean regions with a lower La/Co ratio than that in the La-rich regions (Fig. 4f and Table 1); this is rational as Ca substitutes La at A sites. After 1000 cycles, pronounced Ca loss was observed in the La-lean regions, Fig. 4g-h. In contrast, Ca concentration remained higher in the La-rich regions (Fig. 4h). These results infer that Ca dissolution mainly occurs in the La-lean regions, where the surface is enriched with the B-site cation Co. Additionally, the O concentration in La-lean (also Ca-lean) region increases to ~ 56.9 at.% along with enhanced incorporation of hydroxide ions (Fig. 4h, Table 1). This implies that the oxygen vacancies created by the Ca doping in $LaCoO_3$ potentially promote faster oxygen ion diffusion than that in $LaCoO_3$, contributing to the incorporation and intercalation of hydroxide ions in the bulk of Ca-0.87 % doped $LaCoO_3$ during OER.

Overall, our study provides unprecedented insights into the structural and compositional changes of $LaCoO_3$ and Ca-doped $LaCoO_3$ perovskites, before and after 1000 CV cycles, with sub-nm spatial resolution (see schematic diagram in Fig. 5). Our first important observation is that pristine $LaCoO_3$ are predominantly composed of trivalent La cations (at A-sites) (Fig. 5a). Obtaining information about surface termination using X-ray-based techniques [56,57] or TEM/EDS is challenging due to their limited spatial resolution (see TEM/EDS data in Fig. S2). Our APT data reveals that, the prepared $LaCoO_3$ nanoparticles are terminated by A-site cations (La), which is crucial for density functional theory simulation studies as varying surface terminations (A or B-site) can result in completely different activity. Additionally, we unveil that Ca dopants are incorporated heterogeneously across the $LaCoO_3$ perovskite nanoparticles (Fig. 5c), possibly driven by a combination of electrostatic and elastic interactions arising from the size and charge mismatch of the substituted cation [58,59].

More importantly, our unique multimodal approach provides mechanistic insights into the correlation of structure, composition, and electrochemical performance of perovskites towards OER. We provided direct evidence on the distribution of hydroxide ions in perovskites. Specifically, our APT data reveals that hydroxide ions are present across the entire Ca-0.87 % doped $LaCoO_3$ nanoparticle after OER, which is in contrast to $LaCoO_3$, where hydroxide ions are primarily located at the surface (Fig. 4c, g). Our XPS, TEM and SAED results infer that the enhanced amounts of hydroxide ions on the surface of $LaCoO_3$ is associated with the formation of amorphous $La(OH)_3$, which deteriorates OER activity significantly (Fig. 5b). For Ca-0.87 % doped $LaCoO_3$, the oxygen vacancies promote the fast oxygen ion diffusion and enhanced oxygen intercalation/de-intercalation process (Supplementary Note 1). The hydroxide ions can dynamically replenish the oxygen vacancies in Ca-0.87 % doped $LaCoO_3$, which plays an essential role in retaining the high OER activity of Ca-0.87 % doped $LaCoO_3$ (Fig. 5d). One might speculate that the high activity of Ca-0.87 % doped $LaCoO_3$ is possibly due to the surface transformation of an active CoO_xH_y layer during OER cycles [31]. This is likely to occur but our TEM image (Fig. 3d,f and Fig. S11) and diffraction SAED (Fig. S12d) recorded from hundreds of nanoparticles) did not show the surface of Ca-0.87 % doped $LaCoO_3$ turns into amorphous or new phases formed after 1000 CV cycles. Also, the formation of CoO_xH_y species would lead to the enrichment of

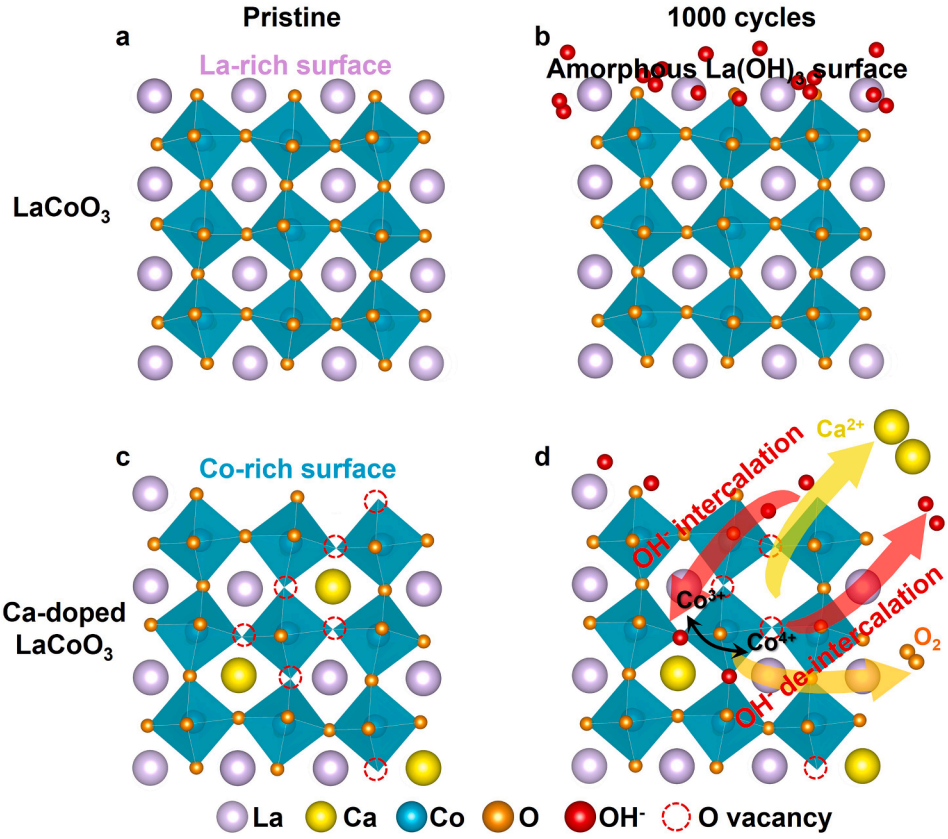

Fig. 5. Schematic diagram of $LaCoO_3$ and Ca-doped $LaCoO_3$ before and after OER. (a, c) the surface of $LaCoO_3$ is terminated by A-site (La) cations, while the surface of Ca-0.87 % doped $LaCoO_3$ is terminated by B-site (Co) cations. After OER, (b) $LaCoO_3$ undergoes surface amorphization due to La dissolution and oxygen loss. In contrast, (d) the surface of Ca-doped $LaCoO_3$ remains crystalline, arisen from dynamic replenishment of hydroxide ions, which promotes the stability. Additionally, a highly reversible Co(+III) ↔ Co(+III, +IV) redox couple appears due to the generation of (c) oxygen vacancies after Ca doping, which enhances the activity of Ca-0.87 % doped $LaCoO_3$.

hydroxide ions on the nanoparticle surfaces, which is inconsistent with our observation that the hydroxide ions are distributed across the entire Ca-0.87 % doped $LaCoO_3$ nanoparticles (see Fig. 4g). Nonetheless, we cannot excluded the possibility as we speculate that surface transformation of the Ca-doped $LaCoO_3$ into $CoO_x(OH)_y$ likely occurs, but highly reversibly [50], making capturing this layer by ex-situ TEM challenging after OER. Additionally, previous works reported that higher Co-O covalency is responsible for the higher OER activity of $La_{0.6}Sr_{0.4}CoO_3$ than $LaCoO_3$ [60]. While the intrinsic activity of perovskites is dominated by metal–oxygen covalency [60,61], oxygen vacancies are thought to be crucially important for intercalation and penetration of hydroxide ions that can preserve the reversibility of the redox couple of the B-site cation (Co). Therefore, the enhanced intercalation and penetration of hydroxide ions, coupled with the highly reversible Co(+III) ↔ Co(+III, +IV) transition, enables the Ca-doped $LaCoO_3$ to maintain higher OER activity within increasing cycles. Notably, such phenomena are directly associated with the superior pseudocapacitor characteristics of perovskite when oxygen vacancies are created, as has been reported in many recent studies [33,62]. Therefore, it is thought that perovskites with pseudocapacitive-type intercalation possibly exhibit superior activity and high OER stability, as observed in Si-doped $SrCoO_3$ and NiCoFe hydroxides [13,63].

4. Conclusion

With the multimodal approach, we can now correlate perovskites' surface structural and compositional changes with their electrocatalytic performance during OER, thereby elucidating the activation and deactivation mechanisms. The unique atomic-scale data demonstrated that oxygen vacancies in $LaCoO_3$ after Ca doping can promote activity and stability towards OER. Our multimodal approach, centered around APT, will be extended to provide mechanistic insights into the structure–activity-stability relationship of numerous metallic and oxides electrocatalysts for other electrocatalytic reactions, such as electrocatalytic CO_2 reduction and oxygen reduction reactions.

CRediT authorship contribution statement

Fan Bai: Writing – original draft, Validation, Investigation, Formal analysis, Data curation, Conceptualization. **Jonas Schulwitz:** Writing – review & editing, Validation, Investigation. **Tatiana Priamushko:** Writing – review & editing, Methodology, Formal analysis. **Ulrich Hagemann:** Writing – review & editing, Validation, Investigation. **Aleksander Kostka:** Writing – review & editing, Validation, Investigation. **Markus Heidelmann:** Writing – review & editing, Validation, Investigation. **Serhiy Cherevko:** Writing – review & editing, Resources, Methodology, Formal analysis. **Martin Muhler:** Writing – review & editing, Resources, Investigation. **Tong Li:** Writing – review & editing, Supervision, Resources, Methodology, Investigation, Funding acquisition, Conceptualization.

Declaration of competing interest

The authors declare that they have no known competing financial interests or personal relationships that could have appeared to influence the work reported in this paper.

Data availability

Data will be made available on request.

Acknowledgements

The authors thank funding from the Deutsche Forschungsgemeinschaft (DFG, German Research Foundation) – Projektnummer 388390466 – TRR 247 (A01, B09 and S projects). F.B. and T.L. thank Zentrum für Grenzflächendominierte Höchstleistungswerkstoffe (ZGH) at Ruhr University Bochum for the access of infrastructure (Cameca LEAP 5000 XR, FEI Helios G4 CX SEM/FIB and JEOL JEM-ARM200F NEOARM). The authors acknowledge Christian Göllner for the technical support during the ICP-MS measurements, Tobias Falk for H_2 TPR measurements, and Noushin Arshadi for N_2 adsorption measurements.

Appendix A. Supplementary data

Supplementary data to this article can be found online at https://doi.org/10.1016/j.jcat.2024.115697.

References

[1] B. Dudley. BP statistical review of world energy, 2018. London.
[2] M. Grätzel, Photoelectrochemical cells, Nature 414 (2001) 338–344.
[3] V.R. Stamenkovic, D. Strmcnik, P.P. Lopes, N.M. Markovic, Energy and fuels from electrochemical interfaces, Nat. Mater. 16 (2017) 57–69.
[4] F.Y. Cheng, J. Chen, Metal-air batteries: from oxygen reduction electrochemistry to cathode catalysts, Chem. Soc. Rev. 41 (2012) 2172–2192.
[5] N.T. Suen, S.F. Hung, Q. Quan, N. Zhang, Y.J. Xu, H.M. Chen, Electrocatalysis for the oxygen evolution reaction: recent development and future perspectives, Chem. Soc. Rev. 46 (2017) 337–365.
[6] J. Suntivich, K.J. May, H.A. Gasteiger, J.B. Goodenough, Y. Shao-Horn, A Perovskite Oxide optimized for oxygen evolution catalysis from molecular orbital principles, Science 334 (2011) 1383–1385.
[7] C. Sun, J.A. Alonso, J. Bian, Recent Advances in Perovskite-Type oxides for energy conversion and storage applications, Adv. Energy Mater. 11 (2020) 2000459.
[8] S. Malkhandi, P. Trinh, A.K. Manohar, A. Manivannan, M. Balasubramanian, G.K. S. Prakash, S.R. Narayanan, Design Insights for Tuning the Electrocatalytic activity of perovskite oxides for the oxygen evolution reaction, J. Phys. Chem. C 119 (2015) 8004–8013.
[9] N.L. Wu, W.R. Liu, S.J. Su, Effect of oxygenation on electrocatalysis of La0.6Ca0.4CoO3-x in bifunctional air electrode, Electrochim. Acta 48 (2003) 1567–1571.
[10] J.T. Mefford, X. Rong, A.M. Abakumov, W.G. Hardin, S. Dai, A.M. Kolpak, K. P. Johnston, K.J. Stevenson, Water electrolysis on La1-xSrxCoO3-delta perovskite electrocatalysts, Nat. Commun. 7 (2016) 11053.
[11] A. Kahoul, A. Hammouche, G. Poillerat, R.W. De Doncker, Electrocatalytic activity and stability of La(1–x)Ca(x)CoO3 perovskite-type oxides in alkaline medium, Catal. Today 89 (2004) 287–291.
[12] K.J. May, C.E. Carlton, K.A. Stoerzinger, M. Risch, J. Suntivich, Y.L. Lee, A. Grimaud, Y. Shao-Horn, Influence of oxygen evolution during water oxidation on the surface of perovskite oxide catalysts, J. Phys. Chem. Lett. 3 (2012) 3264–3270.
[13] Y.L. Pan, X.M. Xu, Y.J. Zhong, L. Ge, Y.B. Chen, J.P.M. Veder, D.Q. Guan, R. O'Hayre, M.R. Li, G.X. Wang, H. Wang, W. Zhou, Z.P. Shao, Direct evidence of boosted oxygen evolution over perovskite by enhanced lattice oxygen participation, Nat. Commun. 11 (2020) 2002.
[14] B.H. Han, A. Grimaud, L. Giordano, W.T. Hong, O. Diaz-Morales, L. Yueh-Lin, J. Hwang, N. Charles, K.A. Stoerzinger, W.L. Yang, M.T.M. Koper, Y. Shao-Horn, Iron-Based perovskites for catalyzing oxygen evolution reaction, J. Phys. Chem. C 122 (2018) 8445–8454.
[15] T. Li, A. Devaraj, N. Kruse, Perspective Atomic-scale characterization of (electro-) catalysts and battery materials by atom probe tomography, Cell Rep. Phys. Sci. 3 (2022).
[16] C.L. Luan, J. Angona, A.B. Krishnan, M. Corva, P. Hosseini, M. Heidelmann, U. Hagemann, E.B. Tetteh, W. Schuhmann, K. Tschulik, T. Li, Linking composition, structure and thickness of CoOOH layers to Oxygen evolution reaction activity by correlative microscopy, Angew. Chem. Int. Edit. 62 (2023) e202305982.
[17] C.L. Luan, M. Corva, U. Hagemann, H.C. Wang, M. Heidelmann, K. Tschulik, T. Li, Atomic-Scale insights into morphological, Structural, and Compositional Evolution of CoOOH during Oxygen Evolution Reaction, ACS Catal. 13 (2023) 1400–1411.
[18] W. Xiang, N. Yang, X. Li, J. Linnemann, U.R. Hagemann, O., M.F. Heidelmann, T. , M. Aramini, S. DeBeer, M. Muhler, K. Tschulik, T. Li, 3D atomic-scale imaging of mixed Co-Fe spinel oxide nanoparticles during oxygen evolution reaction, Nat. Commun. 13 (2022) 179.
[19] A. BalaKrishnan, N. Blanc, U. Hagemann, P. Gemagami, K. Wonner, K. Tschulik, T. Li, Direct Detection of surface species formed on iridium electrocatalysts during the oxygen evolution reaction, Angew. Chem. Int. Edit. 60 (2021) 21396–21403.
[20] J. Zhang, T. Quast, W.H. He, S. Dieckhöfer, J.R.C. Junqueira, D. Öhl, P. Wilde, D. Jambrec, Y.T. Chen, W. Schuhmann, In Situ Carbon Corrosion and Cu Leaching as a strategy for boosting oxygen evolution reaction in multimetal electrocatalysts, Adv. Mater. 34 (2022) 2109108.
[21] T.Z. Wu, S.N. Sun, J.J. Song, S.B. Xi, Y.H. Du, B. Chen, W.A. Sasangka, H.B. Liao, C. L. Gan, G.G. Scherer, L. Zeng, H.J. Wang, H. Li, A. Grimaud, Z.J. Xu, Iron-facilitated dynamic active-site generation on spinel CoAl2O4 with self-termination of surface reconstruction for water oxidation, Nat. Catal. 2 (2019) 763–772.
[22] F.P. Zhao, Z.Q. Yang, Z.S. Wei, R. Spinney, M. Sillanpää, J.T. Tang, M. Tam, R. Y. Xiao, Polyethylenimine-modified chitosan materials for the recovery of La(III) from leachates of bauxite residue, Chem. Eng. J. 388 (2020).

[23] Z.Y. Yu, Z.X. Cheng, X.L. Wang, S.X. Dou, X.Y. Kong, High area-specific capacitance of Co(OH)2/hierarchical nickel/nickel foam supercapacitors and its increase with cycling, J. Mater. Chem. A 5 (2017) 7968–7978.
[24] W.B. Euler, L.J. Kirschenbaum, B. Ruekberg, Determination of Ksp, ΔG0, ΔH0, and ΔS0 for the dissolution of calcium hydroxide in water, J. Chem. Educ. 77 (2000) 1039.
[25] P.M. Raccah, J.B. Goodenough, First-Order localized-electron ⇆ collective-electron transition in LaCoO3, Phys. Rev. 155 (1967) 932.
[26] N.A. Merino, B.P. Barbero, P. Grange, L.E. Cadus, La1-xCaxCoO3 perovskite-type oxides: preparation, characterisation, stability, and catalytic potentiality for the total oxidation of propane, J. Catal. 231 (2005) 232–244.
[27] H.L. Chen, G.L. Wei, X.L. Liang, P. Liu, Y.F. Xi, J.X. Zhu, Facile surface improvement of LaCoO3 perovskite with high activity and water resistance towards toluene oxidation: Ca substitution and citric acid etching, Catal, Sci. Technol. 10 (2020) 5829–5839.
[28] R.D. Shannon, Revised Effective Ionic-Radii and systematic studies of interatomic distances in halides and chalcogenides, Acta Crystallogr. A 32 (1976) 751–767.
[29] P.M. Shafi, N. Joseph, A. Thirumurugan, A.C. Bose, Enhanced electrochemical performances of agglomeration-free LaMnO3 perovskite nanoparticles and achieving high energy and power densities with symmetric supercapacitor design, Chem. Eng. J. 338 (2018) 147–156.
[30] B. Gault, A. Chiaramonti, O. Cojocaru-Miredin, P. Stender, R. Dubosq, C. Freysoldt, S.K. Makineni, T. Li, M. Moody, J.M. Cairney, Atom probe tomography, Nat. Rev. Method. Prime. 1 (2021).
[31] P.P. Lopes, D.Y. Chung, X. Rui, H. Zheng, H.Y. He, P.F.B.D. Martins, D. Strmcnik, V. R. Stamenkovic, P. Zapol, J.F. Mitchell, R.F. Klie, N.M. Markovic, Dynamically stable active sites from surface evolution of perovskite materials during the oxygen evolution reaction, J. Am. Chem. Soc. 143 (2021) 2741–2750.
[32] L. Twight, A. Tonsberg, S. Samira, K. Velinkar, K. Dumpert, Y. Ou, L. Wang, E. Nikolla, S.W. Boettcher, Trace Fe activates perovskite nickelate OER catalysts in alkaline media via redox-active surface Ni species formed during electrocatalysis, J. Catal. 432 (2024).
[33] G.L. Guo, K. Ouyang, J.P. Yu, Y.H. Liu, S.L. Feng, M.R. Wei, Facile Synthesis of LaCoO3 with a high oxygen vacancy concentration by the plasma etching technique for high-performance oxygen ion intercalation pseudocapacitors, ACS Appl. Energy Mater. 3 (2020) 300–308.
[34] J.M. Qian, J.F. Li, B.R. Xia, J.Y. Zhang, Z.M. Zhang, C. Guan, D.Q. Gao, W. Huang, Multi-stability modulating of alkaline-earth metal doped LaCoO3 for rechargeable Zn-air batteries, Energy Storage Mater. 42 (2021) 470–476.
[35] Y. Lu, A.J. Ma, Y.F. Yu, R. Tan, C.W. Liu, P. Zhang, D. Liu, J.Z. Gui, Engineering oxygen vacancies into LaCoO3 perovskite for efficient electrocatalytic oxygen evolution, ACS Sustainable Chem. Eng. 7 (2019) 2906–2910.
[36] A. Moysiadou, S. Lee, C.S. Hsu, H.M. Chen, X.L. Hu, Mechanism of Oxygen evolution Catalyzed by Cobalt Oxyhydroxide: cobalt superoxide species as a key intermediate and dioxygen release as a rate-determining step, J. Am. Chem. Soc. 142 (2020) 11901–11914.
[37] J.Z. Huang, H.Y. Sheng, R.D. Ross, J.C. Han, X.J. Wang, B. Song, S. Jin, Modifying redox properties and local bonding of Co3O4 by CeO2 enhances oxygen evolution catalysis in acid, Nat. Commun. 12 (2021) 3036.
[38] H.Y. Li, Y.B. Chen, J.J. Ge, X.H. Liu, A.C. Fisher, M.P. Sherburne, J.W. Ager, Z. J. Xu, Active Phase on SrCo1-xFexO3−δ ($0 \leq x \leq 0.5$) Perovskite for water oxidation: reconstructed surface versus remaining bulk, Jacs Au 1 (2021) 108–115.
[39] R. Dudric, A. Vladescu, V. Rednic, M. Neumann, I.G. Deac, R. Tetean, XPS study on La0.67Ca0.33Mn1-xCoxO3 compounds, J. Mol. Struct. (2014, 1073,) 66–70.
[40] D.F. Mullica, C.K. Lok, H.O. Perkins, V.V. Young, X-ray photoelectron final-state screening in La(OH)3: a multiplet structural analysis, Phys. Rev. B 31 (1985) 4039–4042.
[41] M.F. Sunding, K. Hadidi, S. Diplas, O.M. Lovvik, T.E. Norby, A.E. Gunnæs, XPS characterisation of in situ treated lanthanum oxide and hydroxide using tailored charge referencing and peak fitting procedures, J. Electron. Spectrosc. 184 (2011) 399–409.
[42] M.L. Weber, G. Lole, A. Kormanyos, A. Schwiers, L. Heymann, F.D. Speck, T. Meyer, R. Dittmann, S. Cherevko, C. Jooss, C. Baeumer, F. Gunkel, Atomistic insights into activation and degradation of La0.6Sr0.4CoO3-δ electrocatalysts under oxygen evolution conditions, J. Am. Chem. Soc. 144 (2022) 17966–17979.
[43] Q.Q. Ji, L. Bi, J.T. Zhang, H.J. Cao, X.S. Zhao, The role of oxygen vacancies of ABO (3) perovskite oxides in the oxygen reduction reaction, Energ. Environ. Sci. 13 (2020) 1408–1428.
[44] H.N. Sun, J. Dai, W. Zhou, Z.P. Shao, Emerging strategies for developing high-performance perovskite-based materials for electrochemical water splitting, Energy Fuels 34 (2020) 10547–10567.
[45] P.W. Menezes, A. Indra, A. Bergmann, P. Chernev, C. Walter, H. Dau, P. Strasser, M. Driess, Uncovering the prominent role of metal ions in octahedral versus tetrahedral sites of cobalt-zinc oxide catalysts for efficient oxidation of water, J. Mater. Chem. A 4 (2016) 10014–10022.
[46] M. Oku, K. Hirokawa, X-Ray Photoelectron-Spectroscopy of Co3O4, Fe3O4, Mn3O4 and Related compounds, J. Electron. Spectrosc. 8 (1976) 475–481.
[47] B.H. Han, M. Risch, Y.L. Lee, C. Ling, H.F. Jia, Y. Shao-Horn, Activity and stability trends of perovskite oxides for oxygen evolution catalysis at neutral pH, Phys. Chem. Chem. Phys. 17 (2015) 22576–22580.
[48] S. Geiger, O. Kasian, M. Ledendecker, E. Pizzutilo, A.M. Mingers, W.T. Fu, O. Diaz-Morales, Z.Z. Li, T. Oellers, L. Fruchter, A. Ludwig, K.J.J. Mayrhofer, M.T. M. Koper, S. Cherevko, The stability number as a metric for electrocatalyst stability benchmarking, Nat. Catal. 1 (2018) 508–515.
[49] T. Wiegmann, I. Pacheco, F. Reikowski, J. Stettner, C. Qiu, M. Bouvier, M. Bertram, F. Faisal, O. Brummel, J. Libuda, J. Drnec, P. Allongue, F. Maroun, O. M. Magnussen, Operando identification of the reversible skin layer on Co(3)O(4) as a Three-Dimensional reaction zone for oxygen evolution, ACS Catal. 12 (2022) 3256–3268.
[50] A. Bergmann, E. Martinez-Moreno, D. Teschner, P. Chernev, M. Gliech, J.F. de Araujo, T. Reier, H. Dau, P. Strasser, Reversible amorphization and the catalytically active state of crystalline Co3O4 during oxygen evolution, Nat. Commun. 6 (2015) 8625.
[51] T. Li, O. Kasian, S. Cherevko, S. Zhang, S. Geiger, C. Scheu, P. Felfer, D. Raabe, B. Gault, K.J.J. Mayrhofer, Atomic-scale insights into surface species of electrocatalysts in three dimensions, Nat. Catal. 1 (2018) 300–305.
[52] B. Bialobok, J. Trawczynski, W. Mista, M. Zawadzki, Ethanol combustion over strontium- and cerium-doped LaCoO3 catalysts, Appl. Catal. B-Environ. 72 (2007) 395–403.
[53] J. Buker, B. Alkan, Q. Fu, W. Xia, J. Schulwitz, D. Waffel, T. Falk, C. Schulz, H. Wiggers, M. Muhler, B.X. Peng, Selective cyclohexene oxidation with O-2, H2O2 and tert-butyl hydroperoxide over spray-flame synthesized LaCo1-xFexO3 nanoparticles, Catal. Sci. Technol. 10 (2020) 5196–5206.
[54] M. Pourbaix, Atlas of electrochemical equilibria in aqueous solutions, NACE, 1974.
[55] S. Samira, X.K. Gu, E. Nikolla, Design strategies for efficient nonstoichiometric mixed metal oxide electrocatalysts: correlating measurable oxide properties to electrocatalytic performance, ACS Catal. 9 (2019) 10575–10586.
[56] S.Z. Song, J. Sun, J. Zhou, C.Z. Guan, Z.W. Hu, T.S. Chan, X.L. Du, X. Lin, J. Hu, L. J. Zhang, J.Q. Wang, Growth of LaCoO3 crystals in molten salt: effects of synthesis conditions, CrstEngComm 23 (2021) 671–677.
[57] N. Orlovskaya, D. Steinmetz, S. Yarmolenko, D. Pai, J. Sankar, J. Goodenough, Detection of temperature- and stress-induced modifications of LaCoO3 by micro-Raman spectroscopy, Phys. Rev. B 72 (2005).
[58] H.P. Ding, A.V. Virkar, M.L. Liu, F. Liu, Suppression of Sr surface segregation in La (1–x)Sr(x)Co(1-y)Fe(y)O(3-delta): a first principles study, Phys. Chem. Chem. Phys. 15 (2013) 489–496.
[59] W. Lee, J.W. Han, Y. Chen, Z.H. Cai, B. Yildiz, Cation size mismatch and charge interactions drive dopant segregation at the surfaces of manganite perovskites, J. Am. Chem. Soc. 135 (2013) 7909–7925.
[60] L. Heymann, M.L. Weber, M. Wohlgemuth, M. Risch, R. Dittmann, C. Baeumer, F. Gunkel, Separating the effects of band bending and covalency in hybrid perovskite oxide electrocatalyst bilayers for water electrolysis, ACS Appl. Mater. Interfaces 14 (2022) 14129–14136.
[61] S. Yagi, I. Yamada, H. Tsukasaki, A. Seno, M. Murakami, H. Fujii, H. Chen, N. Umezawa, H. Abe, N. Nishiyama, S. Mori, Covalency-reinforced oxygen evolution reaction catalyst, Nat. Commun. 6 (2015) 8249.
[62] J.T. Mefford, W.G. Hardin, S. Dai, K.P. Johnston, K.J. Stevenson, Anion charge storage through oxygen intercalation in LaMnO3 perovskite pseudocapacitor electrodes, Nat. Mater. 13 (2014) 726–732.
[63] W.J. Liu, X. Hu, H.C. Li, H.Q. Yu, Pseudocapacitive Ni-Co-Fe Hydroxides/N-Doped carbon nanoplates-based electrocatalyst for efficient oxygen evolution, Small 14 (2018) 1801878.